FINITE ELEMENT IMPLEMENTATION OF NONLINEAR CONSTITUTIVE MODELS FOR PIEZOCERAMIC MATERIALS

Bernd Laskewitz and Marc Kamlah

FINITE ELEMENT IMPLEMENTATION OF NONLINEAR CONSTITUTIVE MODELS FOR PIEZOCERAMIC MATERIALS

BERND LASKEWITZ AND MARC KAMLAH

The objective of this work was the finite element implementation of constitutive material models for piezoceramic materials. A phenomenological material model was implemented by means of a customized radial return mapping algorithm into an open source finite element program, and the problem was reduced to the solution of a single nonlinear algebraic equation. This led to a significant reduction in computation time for simulations compared to an implementation by means of an explicit higher order integration scheme for the constitutive differential equations. Furthermore, a microscopically motivated material model was implemented by means of a radial return mapping algorithm based on the backward Euler scheme.

Apart from simulations of the principal behavior of the material models and their finite element implementations, simulations of applied examples are discussed which demonstrate the properties of the models and the performance of the implementations.

1. Introduction

The *piezoelectric* effect describes a linear relationship between strain and polarization on the one hand, and electric field and stress on the other. Nowadays, this effect is commonly utilized by a class of ferroelectric ceramics, also called piezoceramics for short. The electromechanical coupling properties of these polycrystalline materials are caused by distinct features of their perovskite microstructure. Below the Curie temperature, each grain possesses a substructure of *domains*, these being regions of uniform orientation of the microdipoles of the crystallographic unit cells. Upon application of electric fields and mechanical stresses of sufficient magnitude, the domains can be reoriented. The macroscopic hysteresis properties resulting from microscopic domain switching processes under a cyclic electric field and mechanical stress loading in such a *ferroelectric* material are called *ferroelectricity* and *ferroelasticity*, respectively. In particular, the so-called poling process caused by strong electric fields leads to the orientation of the domains in the direction of the field resulting in a macroscopic piezoelectric effect from the microscopic piezoelectric contributions of the domains.

Piezoceramic materials are used for actuation in various technical fields requiring challenging properties. They facilitate highly accurate positioning, show fast response times, and allow for large actuation forces. Examples of technical applications are diesel injection valves (which in 2005 won the Deutscher Zukunftspreis awarded by the President of the Federal Republic of Germany[1]), as well as positioners in nano- and microtechnology.

[1]See announcement at http://www.deutscher-zukunftspreis.de/en/nominierter/piezo-injectors-new-technologybr-clean-and-economical-diesel-and-gasoline-engines

The composition of piezoceramic materials is subject to constant improvement in optimizing the piezo-electric properties. On the other hand, with respect to modeling, in commercial finite element codes only a linear relationship between the quantities is taken into account for simulation of the electromechanical behavior. As an important example, the above mentioned poling process and the resulting residual stresses after poling as part of manufacturing piezoelectric devices made of ferroelectrics cannot be simulated. Furthermore, mechanical depolarization cannot be taken into account in computations based on linear piezoelectric behavior. This lack of capability to represent the electromechanical fields correctly leads to increasing difficulties in predicting malfunctions and failures of devices in complex applications. The current paper deals with providing such finite element tools taking into account the complete spectrum of electromechanically coupled large signal hysteresis behavior of ferroelectrics. Such tools are needed as basis for the assessment of the reliability of piezoceramic devices, for example.

This paper is organized as follows: In Section 2, the literature regarding constitutive modeling of piezoceramic materials and finite element implementations will be reviewed. At the beginning of Section 3, the phenomenological constitutive model developed earlier will be described [Kamlah and Tsakmakis 1999; Kamlah 2001; Kamlah and Boehle 2001]. The finite element tool described in these papers is among the very earliest capable of taking into account the complete coupled ferroelectric and ferroelastic large signal hysteresis properties of piezoceramics. On the other hand, the implementation algorithm, based on a higher order explicit integration scheme for the constitutive differential equations, lacked computational efficiency.

In the first main section (Section 3) we present a significantly improved integration algorithm for the phenomenological constitutive model in the open source finite element code PSU [PSU 2000]. This implementation is verified by comparing simulated curves to experimentally measured behavior. In addition, the poling of a stack actuator is discussed as a simulation example.

In the second main section (Section 4), we introduce a microscopically motivated material model [Kamlah and Jiang 1999; Kamlah and Wang 2003]. This model operates at the same length scale as the previously mentioned phenomenological model. However, it is based on the orientation distribution function of ferroelectric domains, and its evolution due to domain switching. Thus, it possesses a clear micromechanical foundation. The finite element implementation of this model is based on a backward Euler scheme. Verification examples and an example simulation demonstrate the capability of the obtained computation tool. The computation time is longer due to the complexity of the model and the integration algorithm, but, on the other hand, it can describe poling processes more realistically than the phenomenological model. This leads to a better understanding of the behavior of ferroelectric materials.

2. Constitutive modeling of ferroelectrics

2.1. *Phenomenological approach.* The phenomenological approach is an efficient way to describe the complex behavior of piezoceramic materials. The disadvantages of this approach result from the fact that the material behavior is described phenomenologically which means in general that a calibration is necessary. Outside of the range of loadings considered in developing such a model, there is always the danger that it may be inaccurate or even qualitatively wrong. In the field of phenomenological models some significant improvements have been made since the work of Chen [1980] which will be described subsequently.

McMeeking and Landis [2002] proposed a phenomenological model for ferroelectric switching processes subject to multiaxial mechanical and electrical loadings. It is based on a kinematic hardening theory with a switching surface in the space of stress and electric field. McMeeking and Landis [2002] express the remanent strain by means of a function of remanent polarization. This approach simplifies the model significantly, but excludes purely ferroelastic hysteretic behavior.

Such an restriction does not apply to the model of Landis [2002]. It is based on the Helmholtz free energy of the material. A domain switching surface and flow rules for the internal variables in the space of stress and electric field are introduced. The derived constitutive law has a symmetric material tangent. This leads to faster computation time and lower memory demand for the finite element implementation compared to models which rely on asymmetric tangents.

Huber and Fleck [2001] proposed — in addition to their crystal plasticity type theory [Huber et al. 1998; Huber and Fleck 2004], see Section 2.2 — a phenomenological model. The computation time for this model is short, but it is specialized to nearly uniaxial cyclic loadings.

Kessler and Balke [2001] derived an expression for the local and average energy release rate during polarization orientation processes. On this basis, they developed a repolarization model which can describe pure rotation of the polarization at a fixed magnitude.

Schroeder and Gross [2004] developed a fully coupled electromechanical formulation for transversally isotropic materials for reversible material behavior. A variational and finite element formulation for fully coupled problems with small deformations is presented. Schroeder and Romanowski [2005] enhanced the model with consideration of domain switching to be able to describe fundamental hysteresis effects. However, only the magnitude of polarization can change while its direction is fixed in space, and strain is just a function of polarization.

Belov and Kreher [2005] proposed two viscoplasticity type models without loading conditions for the onset of switching. The evolution of the structure of domains is described by means of rate-dependent equations of the volume fractions of orientation variants. The first model offers six different domain orientations and is proposed for uniaxial loadings. The second model has 42 possible domain orientations and can be applied to multiaxial simulations.

Elhadrouz et al. [2005a; 2005b] used the material law of Kamlah and Boehle [Boehle 1999; Kamlah and Tsakmakis 1999; Kamlah 2001; Kamlah and Boehle 2001]. They coded an element for the finite element implementation of the model in a commercially available finite element code.

Klinkel [2006] has developed on the basis of a thermodynamically consistent approach a 1D model for ferroelastic and ferroelectric hysteresis effects of piezoceramics. He made use of the Helmholtz free energy and a domain switching surface for the thermodynamical framework of his work. As a specific feature, he introduced, besides irreversible strain, an irreversible electric field as a state variable. This simplifies the finite element implementation, but doesn't have an immediate physical interpretation.

2.2. *Micromechanical modeling.* Many available theoretical studies are based on micromechanical material models [Hwang et al. 1995; 1998; Chen et al. 1997; Chen and Lynch 1998; Huber et al. 1998; Hwang 2000; Smith et al. 2003; Huber and Fleck 2004; Seemann et al. 2004; Delibas et al. 2005; Kamlah et al. 2005; Semenov et al. 2006] which have led to a better understanding of the behavior of ferroelectrics. In general an application of micromechanical models to common engineering problems is difficult because the models are mostly very complex and computationally expensive. But, they have

significant advantages compared to phenomenological models because the range of validity of microme-
chanical models is mostly more general as basic mechanisms on the microscopic level are taken into
consideration.

On the basis of the constitutive behavior of single crystals Chen and Lynch [1998] have developed a
micromechanical model for polycrystalline, ferroelectric ceramics. The model simulates tetragonal and
rhombohedral crystal structures in which a saturation of the linear piezoelectric effect is implemented.
Furthermore the interaction between the different grains of the polycrystal is considered. A switching
criterion was developed which takes into consideration the domain switching processes of the tetragonal
and rhombohedric crystal structure.

Huber et al. [1998] and Huber and Fleck [2004] describe a micromechanical model based on crystal
plasticity theory. A grain is a mixture of variants, a variant representing all domains of equal orientation
of the spontaneous polarization inside a grain. Switching processes transform a variant into another
variant. The polycrystalline properties are then obtained by a self-consistent scheme to yield irreversible
polarization and irreversible strain, as well as the average linear electromechanical properties. In [Kamlah
et al. 2005], grain to grain interaction is modeled explicitly by means of the finite element method.

Seemann et al. [2004] and Delibas et al. [2005] have derived a model on the level of the grains of a
polycrystal in which they assume that after poling the domains in a grain have the same orientation. The
basis of the model is an energetic approach from [Hwang et al. 1998] in which the potential energy of a
single domain is taken into consideration. If the potential energy rises beyond a certain limit, the domain
switches. The response of the polycrystal is the average of all domain processes. Mutual interaction of
domain processes is accounted for by some probabilistic functions.

Smith et al. [2003] developed a micromechanical model on the basis of the Helmholtz and Gibbs free
energy at the lattice level of the crystal structure of a single crystal. The embedding in polycrystalline
structures is carried out by means of a stochastic homogenization to include the inhomogeneous structure
of polycrystals. This model provides an excellent thermodynamical basis to simulate the macroscopic
behavior of ferroelectric polycrystals.

3. Phenomenological material model and its finite element implementation

The phenomenological material model used in this work was developed in [Kamlah and Tsakmakis
1999; Kamlah and Boehle 2001; Kamlah 2001]. Here, we will give only an outline of the basic fea-
tures. The model can describe ferroelectric and ferroelastic hysteresis behavior including mechanical
depolarization and polarization rotation. The finite element implementation reported in [Kamlah and
Boehle 2001] is computationally expensive since it relies on the solution of a system of nine ordinary
differential equations by means of an explicit Runge–Kutta algorithm. Therefore, a customized radial
return mapping algorithm was developed where computing the constitutive model was reduced to solving
a single nonlinear algebraic equation (see also [Laskewitz and Kamlah 2004]). This new implementation
reduced the computation time significantly and made it possible to simulate the poling processes of
structures consisting of tens of thousands of elements.

3.1. *Formulation of the phenomenological material model.* A constitutive model for ferroelectric ma-
terials relates strain S_{ij} and polarization P_i to the histories of stress T_{ij} and electric field E_i [Kamlah
2001]. Analogously to plasticity theory the hysteretic behavior of piezoceramic materials motivates a

decomposition of strain S_{ij} and polarization P_i into reversible and irreversible parts [Zhou et al. 2005a; 2005b]:

$$S_{ij} = S_{ij}^{r} + S_{ij}^{i}, \qquad P_i = P_i^{r} + P_i^{i}. \tag{1}$$

The irreversible parts represent volume averages of spontaneous strain and polarization, respectively, over some representative volume element. The reversible parts are related to the *stress tensor* T_{ij} and the *electric field vector* E_i by

$$S_{ij}^{r} = C_{ijkl}^{-1} T_{kl} + d_{kij} E_k, \qquad P_i^{r} = d_{ijk} T_{jk} + \kappa_{ij} E_j, \tag{2}$$

with C_{ijkl} as the *tensor of elasticity*, d_{ijk} as the *tensor of piezoelectricity* and κ_{ij} as the *tensor of susceptibility*. These equations possess the structure of linear piezoelectricity theory, in which the tensor of piezoelectricity is anisotropic and depends on the loading history in terms of the irreversible polarization P_i^{i}:

$$d_{kij} = \frac{\|P_i^{i}\|}{P^{\mathrm{sat}}} \left\{ d^{\|} e_i e_j e_k + d^{\perp} (\delta_{ij} - e_i e_j) e_k + d^{=} \frac{1}{2} [(\delta_{ki} - e_k e_i) e_j + (\delta_{kj} - e_k e_j) e_i] \right\}. \tag{3}$$

Here, $\|P_i^{i}\| = \sqrt{P_i^{i} P_i^{i}}$ and

$$e_i = \frac{P_i^{i}}{\|P_i^{i}\|} \tag{4}$$

is the unit vector in the direction of irreversible polarization, while the piezoelectric constants can be identified as $d^{\|} = d_{33}$, $d^{\perp} = d_{31}$, $d^{=} = \frac{1}{2} d_{15}$, and P^{sat} is the saturation value of irreversible polarization. We adopt the common simplification of assuming C_{ijkl} and κ_{ij} to be isotropic.

The loading history is represented in terms of irreversible strain S_{ij}^{i} and irreversible polarization P_i^{i} as internal variables. Irreversible strain S_{ij}^{i} is divided according to

$$S_{ij}^{i} = S_{ij}^{ie} + S_{ij}^{im} \tag{5}$$

into electrically and mechanically induced parts. The electrically induced part is given as a function of irreversible polarization as

$$S_{ij}^{ie} = \frac{3}{2} S^{\mathrm{sat}} \frac{\|P_i^{i}\|}{P^{\mathrm{sat}}} \left(e_i e_j - \frac{1}{3} \delta_{ij} \right). \tag{6}$$

As will be sketched in the following, irreversible mechanically induced strain S_{ij}^{im} and irreversible polarization P_i^{i} are computed from evolution equations derived from switching criteria and saturation criteria.

The electrical switching function is expressed by

$$f^{\mathrm{e}}(E_i, P_i^{i}) = \|E_i - c^{\mathrm{e}} P_i^{i}\| - E^{\mathrm{c}}, \tag{7}$$

in which E^{c} and c^{e} are nonnegative material parameters. Condition $f^{\mathrm{e}} = 0$ defines the point where the coercive field is reached and domains begin to switch in the direction of the electric field, that is, irreversible polarization P_i^{i} starts to evolve. The evolution is limited such that the magnitude stays below the saturation polarization $\hat{P}^{\mathrm{sat}}$ with the help of the electrical saturation function

$$h^{\mathrm{e}}(E_i, P_i^{i}, T_{ij}) = \|P_i^{i}\| - \hat{P}^{\mathrm{sat}}(E_i, P_i^{i}, T_{ij}), \tag{8}$$

in accordance with the condition $h^{\mathrm{e}} = 0$. Here, the saturation polarization is defined by

$$\hat{P}^{\mathrm{sat}}(T_{ij}, E_i, P_i^{\mathrm{i}}) = (P^{\mathrm{sat}} - P^\delta)\left\langle 1 - \frac{1}{m}\langle -\tfrac{3}{2}e_i T_{ij}^{\mathrm{D}} e_j - \hat{T}^{\mathrm{c}}\rangle\right\rangle + P^\delta, \tag{9}$$

with the constant $P^\delta \geq 0$ being the part of the remanent polarization which remains after the maximum mechanical depolarization and m a positive material constant. Furthermore, A_{ij}^{D} is the deviator of tensor A_{ij}, while $\langle x \rangle = 0$ for $x \leq 0$ and $\langle x \rangle = x$ for $x \geq 0$.

The mechanical switching function,

$$f^{\mathrm{m}}(E_i, P_i^{\mathrm{i}}, T_{ij}, S_{ij}^{\mathrm{im}}) = \|(T_{ij} - c^{\mathrm{m}} S_{ij}^{\mathrm{im}})^{\mathrm{D}}\| - \hat{T}^{\mathrm{c}}(E_i, P_i^{\mathrm{i}}), \tag{10}$$

is used to define at $f^{\mathrm{m}} = 0$ the point where the coercive stress $\hat{T}^{\mathrm{c}}$ is reached and the evolution of the mechanically induced irreversible strain S_{ij}^{im} is initiated. Here c^{m} is a nonnegative material parameter and $\|A_{ij}\| = \sqrt{A_{ij} A_{ij}}$. The coercive stress depends on the superposed electric field according to

$$\hat{T}^{\mathrm{c}}(E_i, P_i^{\mathrm{i}}) = \left\langle T^{\mathrm{c}} + n\frac{E_i}{E^{\mathrm{c}}}e_i\right\rangle \tag{11}$$

with n as a nonnegative material constant. The mechanical saturation function,

$$h^{\mathrm{m}}(P_i^{\mathrm{i}}, S_{ij}^{\mathrm{im}}) = \sqrt{\tfrac{2}{3}}\|S_{ij}^{\mathrm{im}}\| - \left(S^{\mathrm{sat}} - \sqrt{\tfrac{2}{3}}\|S_{ij}^{\mathrm{ie}}\|\right), \tag{12}$$

is used to limit by the condition $h^{\mathrm{m}} = 0$ the evolution of the total irreversible strain S_{ij}^{i} to the saturation strain S^{sat}.

The irreversible polarization and the irreversible strain are computed by evolution equations which are derived from the normality rule and the consistency condition for the respective active switching or saturation condition. By introducing the notation

$$\lfloor x \rceil = \begin{cases} 1, & x \geq 0, \\ 0, & x < 0, \end{cases} \qquad \lceil x \rfloor = \begin{cases} 1, & x > 0, \\ 0, & x \leq 0, \end{cases} \tag{13}$$

and

$$\overset{*}{f}{}^{\mathrm{e}} = \frac{d}{dt}f^{\mathrm{e}}\Big|_{\dot{P}_i^{\mathrm{i}}=0}, \qquad \overset{*}{h}{}^{\mathrm{e}} = \frac{d}{dt}h^{\mathrm{e}}\Big|_{\dot{P}_i^{\mathrm{i}}=\lfloor f^{\mathrm{e}}\rceil\lfloor\overset{*}{f}{}^{\mathrm{e}}\rceil\lambda_f^{\mathrm{e}}\frac{\partial f^{\mathrm{e}}}{\partial E_i}},$$
$$\overset{*}{f}{}^{\mathrm{m}} = \frac{d}{dt}f^{\mathrm{m}}\Big|_{\dot{S}_{ij}^{\mathrm{i}}=0}, \qquad \overset{*}{h}{}^{\mathrm{m}} = \frac{d}{dt}h^{\mathrm{m}}\Big|_{\dot{S}_{ij}^{\mathrm{i}}=\lfloor f^{\mathrm{m}}\rceil\lfloor\overset{*}{f}{}^{\mathrm{m}}\rceil\lambda_f^{\mathrm{m}}\frac{\partial f^{\mathrm{m}}}{\partial T_{ij}}}, \tag{14}$$

as well as

$$F^{\mathrm{k}} = \lfloor f^{\mathrm{i}}\rceil\lfloor\overset{*}{f}{}^{\mathrm{k}}\rceil, \qquad H^{\mathrm{k}} = \left\lceil\lfloor h^{\mathrm{k}}\rceil\lceil\overset{*}{h}{}^{\mathrm{k}}\rfloor + \lceil f^{\mathrm{k}}\rfloor\right\rceil, \qquad \mathrm{k = e, m}, \tag{15}$$

and finally

$$n_i^{\mathrm{e}} = \frac{\partial h^{\mathrm{e}}/\partial P_i^{\mathrm{i}}}{\|\partial h^{\mathrm{e}}/\partial P_i^{\mathrm{i}}\|}, \qquad N_{ij}^{\mathrm{m}} = \frac{\partial h^{\mathrm{m}}/\partial S_{ij}^{\mathrm{i}}}{\|\partial h^{\mathrm{m}}/\partial S_{ij}^{\mathrm{i}}\|}, \tag{16}$$

the evolution equations for the state variables can be written as

$$\dot{P}_i^{\mathrm{i}} = (\delta_{ij} - H^{\mathrm{e}}n_i^{\mathrm{e}}n_j^{\mathrm{e}})\left(F^{\mathrm{e}}\lambda_f^{\mathrm{e}}\frac{\partial f^{\mathrm{e}}}{\partial E_i}\right) + H^{\mathrm{e}}\lambda_h^{\mathrm{e}}\frac{\partial h^{\mathrm{e}}}{\partial P_i^{\mathrm{i}}}, \tag{17}$$

and

$$\dot{S}_{ij}^{\text{im}} = (\delta_{ik}\delta_{jl} - H^{\text{m}} N_{ij}^{\text{m}} N_{kl}^{\text{m}})\left(F^{\text{m}} \lambda_f^{\text{m}} \frac{\partial f^{\text{m}}}{\partial T_{ij}}\right) + H^{\text{m}} \lambda_h^{\text{m}} \frac{\partial h^{\text{m}}}{\partial S_{ij}^{\text{im}}}. \tag{18}$$

The factors of proportionality λ_f^{e}, λ_h^{e}, λ_f^{m}, and λ_h^{m} are defined by the consistency conditions $\dot{f}^{\text{e}} = 0$, $\dot{h}^{\text{e}} = 0$, $\dot{f}^{\text{m}} = 0$, and $\dot{h}^{\text{m}} = 0$, respectively. For further details on this model, the reader is referred to [Kamlah and Tsakmakis 1999; Kamlah and Boehle 2001; Kamlah 2001].

3.2. *Finite element implementation.* In [Kamlah and Boehle 2001], a finite element implementation of the phenomenological constitutive model sketched in the previous section is presented, where the system (17), (18) is solved by an explicit higher order integration scheme considering all combinations of cases that may occur. This scheme turned out to be too slow and not very reliable. In the following, we will describe a customized radial return mapping algorithm exploiting the hierarchy of switching and saturation criteria.

The electromechanical finite element formulation of Allik and Hughes [1970], which employs displacement and electric potential as primary nodal variables, is used. In the nonlinear finite element method, the loading history is divided into increments. In the following, the indices n and $n+1$ describe the states at the beginning and end of the current increment, respectively. At the beginning of increment n, the state of all variables is known. We assume that trial values $^{n+1}S_{ij}$ and $^{n+1}E_i$ for strain and electric field, respectively, have been computed by the global Newton method. The irreversible polarization $^{n+1}P_i^{\text{i}}$ and mechanically induced strain $^{n+1}S_{ij}^{\text{im}}$ corresponding to the trial values have to be calculated. Once all state variables at the end of the increment are known, $^{n+1}T_{ij}$ and $^{n+1}D_i$ can be computed to check equilibrium, $T_{ij,j} = 0$, and Gauss' law, $D_{i,i} = 0$. Here, $D_i = \varepsilon_0 E_i + P_i$ is the electric displacement and ε_0 is the dielectric constant of vacuum.

In this work, the irreversible polarization and the irreversible strain at the end of the increment are obtained from a two step corrector scheme by

$$^{n+1}P_i^{\text{i}} = {}^nP_i^{\text{i}} + \Delta P_i^{\text{i,f}} + \Delta P_i^{\text{i,h}}, \qquad {}^{n+1}S_{ij}^{\text{im}} = {}^nS_{ij}^{\text{im}} + \Delta S_{ij}^{\text{im,f}} + \Delta S_{ij}^{\text{im,h}}. \tag{19}$$

The correctors $\Delta P_i^{\text{i,f}}$, $\Delta P_i^{\text{i,h}}$, $\Delta S_{ij}^{\text{im,f}}$, and $\Delta S_{ij}^{\text{im,h}}$ of irreversible polarization and mechanically induced irreversible strain in the radial return mapping algorithm are obtained from the corresponding electric and mechanical switching and saturation criteria, respectively. The calculation of the correctors for the example of irreversible polarization is explained with the help of Table 1 and Figure 1.

First, the criterion for the onset of electrically induced domain switching according to Equation (7) is checked. For $f^{\text{e}}(^{n+1}E_i, {}^nP_i^{\text{i}}) \leq 0$, no switching occurs and, thus, there is no evolution of irreversible polarization in the current load step, that is, $\Delta P_i^{\text{i,f}} = 0$. For $f^{\text{e}}(^{n+1}E_i, {}^nP_i^{\text{i}}) > 0$, the trial value $^{n+1}E_i$ for the electric field violates the electric switching criterion, and a nontrivial corrector $\Delta P_i^{\text{i,f}}$ needs to be calculated such that $f^{\text{e}}(^{n+1}E_i, {}^nP_i^{\text{i}} + \Delta P_i^{\text{i,f}}) = 0$ is satisfied. According to the first term in (17), we make the ansatz that the corrector $\Delta P_i^{\text{i,f}}$ is in the direction normal to the electric switching criterion. The normal is calculated on the basis of the trial value for the electric field and irreversible polarization from the last load step,

$$\Delta P_i^{\text{i,f}} = \alpha^{\text{e}} \frac{\partial f^{\text{e}}(^{n+1}E_i, {}^nP_i^{\text{i}})}{\partial E_i}, \tag{20}$$

Criterion	Ansatz for corrector	Condition for magnitude
Onset of switching		
$f^{\mathrm{e}}(^{n+1}E_i, {}^{n}P_i^{\mathrm{i}}) \leq 0$	$\Delta P_i^{\mathrm{i,f}} = 0$	
$f^{\mathrm{e}}(^{n+1}E_i, {}^{n}P_i^{\mathrm{i}}) > 0$	$\Delta P_i^{\mathrm{i,f}} = \alpha^{\mathrm{e}} \dfrac{\partial f^{\mathrm{e}}(^{n+1}E_i, {}^{n}P_i^{\mathrm{i}})}{\partial E_i}$	$f^{\mathrm{e}}(^{n+1}E_i, {}^{n}P_i^{\mathrm{i}} + \Delta P_i^{\mathrm{i,f}}) = 0$
Saturation		
$h^{\mathrm{e}}(^{n+1}S_{ij}, {}^{n+1}E_i, {}^{n}P_i^{\mathrm{i}} + \Delta P_i^{\mathrm{i,f}}) \leq 0$	$\Delta P_i^{\mathrm{i,h}} = 0$	
$h^{\mathrm{e}}(^{n+1}S_{ij}, {}^{n+1}E_i, {}^{n}P_i^{\mathrm{i}} + \Delta P_i^{\mathrm{i,f}}) > 0$	$\Delta P_i^{\mathrm{i,h}} = \beta^{\mathrm{e}} \dfrac{\partial h^{\mathrm{e}}(^{n+1}S_{ij}, {}^{n+1}E_i, {}^{n}P_i^{\mathrm{i}} + \Delta P_i^{\mathrm{i,f}})}{\partial P_i^{\mathrm{i}}}$	$h^{\mathrm{e}}(^{n+1}S_{ij}, {}^{n+1}E_i, {}^{n}P_i^{\mathrm{i}} + \Delta P_i^{\mathrm{i,f}} + \Delta P_i^{\mathrm{i,h}}) = 0$

Table 1. Conditions for the calculation of the correctors for irreversible polarization. Condition $f^{\mathrm{e}} = 0$ can be solved analytically for α^{e}, while $h^{\mathrm{e}} = 0$ has to be solved numerically for β^{e}.

where the factor of proportionality α^{e} gives the magnitude of the corrector. Plugging this into the condition $f^{\mathrm{e}}(^{n+1}E_i, {}^{n}P_i^{\mathrm{i}} + \Delta P_i^{\mathrm{i,f}}) = 0$ leads to a nonlinear equation which can be solved analytically to yield

$$\alpha^{\mathrm{e}} = \frac{1}{c^{\mathrm{e}}} f^{\mathrm{e}}(^{n+1}E_i, {}^{n}P_i^{\mathrm{i}}), \tag{21}$$

and, thus, the corrector $\Delta P_i^{\mathrm{i,f}}$ is completely determined.

Next, the criterion for the saturation of irreversible polarization according to (8) has to be checked. For this, the stresses have to be eliminated by the trial strains with the help of (1)$_1$, (2), and (5). For $h^{\mathrm{e}}(^{n+1}S_{ij}, {}^{n+1}E_i, {}^{n}P_i^{\mathrm{i}} + \Delta P_i^{\mathrm{i,f}}) \leq 0$, saturation polarization has not yet been reached in the current load step, and, consequently, $\Delta P_i^{\mathrm{i,h}} = 0$. On the other hand, for $h^{\mathrm{e}}(^{n+1}S_{ij}, {}^{n+1}E_i, {}^{n}P_i^{\mathrm{i}} + \Delta P_i^{\mathrm{i,f}}) > 0$, the magnitude of the possibly once corrected polarization vector ${}^{n}P_i^{\mathrm{i}} + \Delta P_i^{\mathrm{i,f}}$ calculated from the trial strain and trial electric field is beyond its stress dependent saturation value. A corresponding corrector $\Delta P_i^{\mathrm{i,h}}$ is calculated from the condition $h^{\mathrm{e}}(^{n+1}S_{ij}, {}^{n+1}E_i, {}^{n}P_i^{\mathrm{i}} + \Delta P_i^{\mathrm{i,f}} + \Delta P_i^{\mathrm{i,h}}) = 0$. For this, we obtain from the second term in evolution (17) the ansatz for corrector $\Delta P_i^{\mathrm{i,h}}$ to be normal to the saturation criterion $h^{\mathrm{e}}(^{n+1}S_{ij}, {}^{n+1}E_i, {}^{n}P_i^{\mathrm{i}} + \Delta P_i^{\mathrm{i,f}}) = 0$ given by the trial values for strain and electric field and the once corrected irreversible polarization vector:

$$\Delta P_i^{\mathrm{i,h}} = \beta^{\mathrm{e}} \frac{\partial h^{\mathrm{e}}(^{n+1}S_{ij}, {}^{n+1}E_i, {}^{n}P_i^{\mathrm{i}} + \Delta P_i^{\mathrm{i,f}})}{\partial P_i^{\mathrm{i}}}. \tag{22}$$

Requiring the saturation criterion to be satisfied yields the nonlinear algebraic equation

$$h^{\mathrm{e}}\left(^{n+1}S_{ij}, {}^{n+1}E_i, {}^{n}P_i^{\mathrm{i}} + \Delta P_i^{\mathrm{i,f}} + \beta^{\mathrm{e}} \frac{\partial h^{\mathrm{e}}(^{n+1}S_{ij}, {}^{n+1}E_i, {}^{n}P_i^{\mathrm{i}} + \Delta P_i^{\mathrm{i,f}})}{\partial P_i^{\mathrm{i}}}\right) = 0, \tag{23}$$

which needs to be solved numerically for the only unknown scalar parameter β^{e}.

In a similar way as just described, correctors $\Delta S_{ij}^{\mathrm{im,f}}$ and $\Delta S_{ij}^{\mathrm{im,h}}$ are computed for the irreversible strain. The corresponding conditions $f^{\mathrm{m}} = 0$ and $h^{\mathrm{m}} = 0$ for α^{m} and β^{m}, respectively, can both be solved analytically. Special care has to be taken, as the two saturation criteria are electromechanically coupled, such that, depending on the loading, they might be considered separately or have to be considered together.
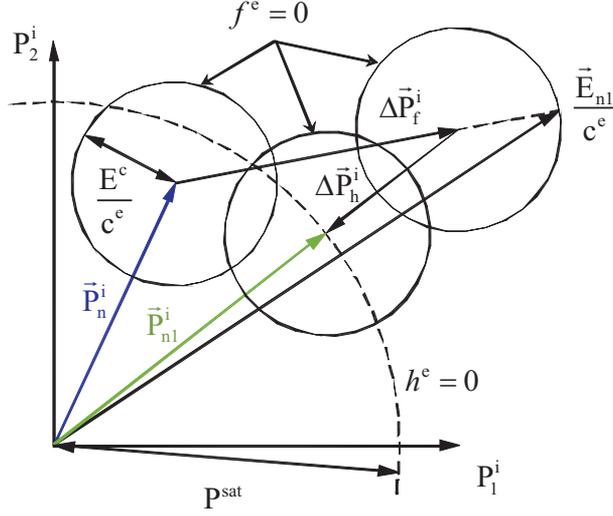
Figure 1. The radial return mapping algorithm used for the finite element implementation of the phenomenological material model for the dielectric hysteresis: In case the predictor $^{n+1}E_i/c^e$ violates the electrical switching condition f^e (the solid circle with irreversible polarization $^nP_i^i$ of the last increment as its center), the corrector $\Delta P_i^{i,f}$ is found. In the situation where all domains are switched into the direction of the electric field, the electrical saturation condition h^e (the dashed circle) becomes active meaning the new predictor $^nP_i^i + \Delta P_i^{i,f}$ has to be checked. If it is outside the saturation condition, an additional corrector $\Delta P_i^{i,h}$ has to be computed which lies on the line of action of $^nP_i^i + \Delta P_i^{i,f}$.

Nevertheless, in any case the problem can be reduced to solving numerically at most a single nonlinear scalar algebraic equation for a single scalar parameter. For the numerical solution, Newton's method and the regula falsi method are used. For the full set of equations including all details on the solution algorithm the reader is referred to [Laskewitz 2007].

3.3. *Verification of the finite element implementation.* This section describes the verification of the material model and its finite element implementation. Simple experiments were carried out [Laskewitz 2007] and compared to simulation results. Table 2 shows the values of the material parameters. Because of the usually ill conditioned electromechanical stiffness matrix, the material parameters are recalculated in units which lead to a better conditioned matrix.

Figure 2 shows the dielectric and the butterfly hysteresis of the simulations and experiments. The corner points of the simulation results represent the electrical switching and saturation conditions of the phenomenological model. A good agreement is observed between the simulation and the experimental results.

3.4. *Simulation example: stack actuator.* To demonstrate the capability of the presented finite element tool a simulation example is presented in this section. It deals with the poling process of a common stack actuator (see Figure 3) which consists of many thin layers with inner electrodes. The basic idea of a stack actuator is to provide large longitudinal displacements at moderate voltages. To reduce the danger of

E^{c} (MV/mm)	1.0×10^{3}
P^{sat} (kN/(MVmm))	310×10^{-3}
σ^{c} (kN/mm^{2})	40.0×10^{-3}
S^{sat}	0.00225
Y (kN/mm^{2})	60.0
ν	0.37
$d^{\parallel}$ (mm/MV)	6.75×10^{-1}
$d^{\perp}$ (mm/MV)	-3.15×10^{-1}
$d^{=}$ (mm/MV)	4.35×10^{-1}
c^{e} (MV^{2}/kN)	1.0×10^{-3}
c^{m} (kN/mm^{2})	20.0
P^{δ} (kN/(MVmm))	100×10^{-3}
n (kN/mm^{2})	20.0×10^{-3}
m (kN/mm^{2})	150×10^{-3}

Table 2. Material parameters used in simulations.
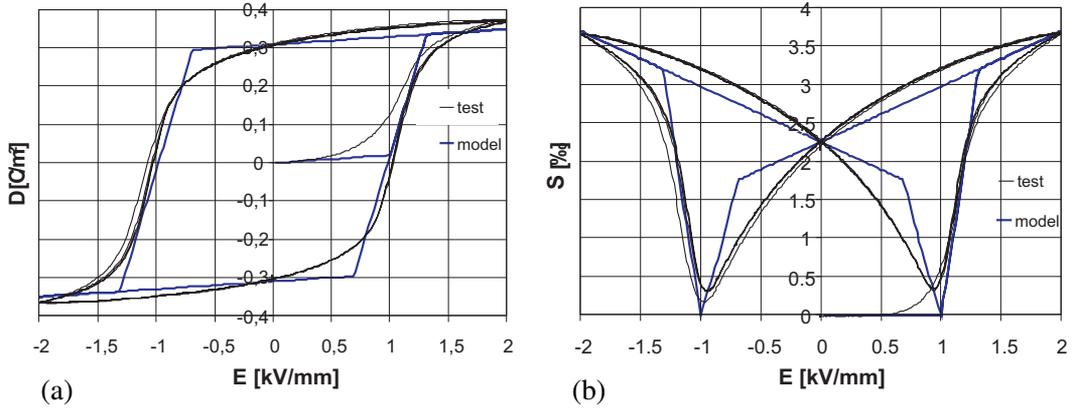
Figure 2. Comparison of simulation results with experiments: (a) dielectric hysteresis and (b) butterfly hysteresis.

electrical arcing and to eliminate the need for a high voltage source, the actuator is composed of a large number of thin piezoceramic layers ($< 100 \, \mu$m) sandwiched between alternately contacted electrodes. The inner electrodes end at a certain distance from the side opposite to the so-called termination electrode by which they are connected to the voltage source. Common usages of stack actuators are diesel injection valves or positioners because of the short response time and the ability for very accurate positioning.

We consider a 2D finite element model representing half of a piezoceramic layer. Figure 3 also shows a sketch of the electric field lines to be expected. The finite element discretization and the geometry are depicted in Figure 4. The model consists of approximately 1000 elements (plane strain). The nodes at the top of the model are coupled to have equal displacement in the vertical direction as a symmetry condition. On the left hand side of the model, we use fixed horizontal displacements as an approximation
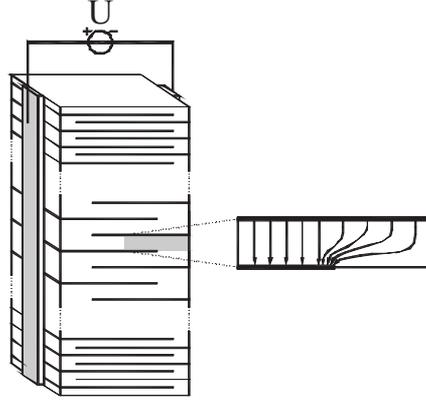
Figure 3. Simplified sketch of a stack actuator.

$$\varphi(t) = 0\mathrm{V}, \; u_2(x_1) = \mathrm{const}, \; \int T_{22}(x_1)dx_1 = 0$$

$\varphi(t) = \hat{\varphi}(t)$

800 µm

1000 µm

50 µm

Location of element 468
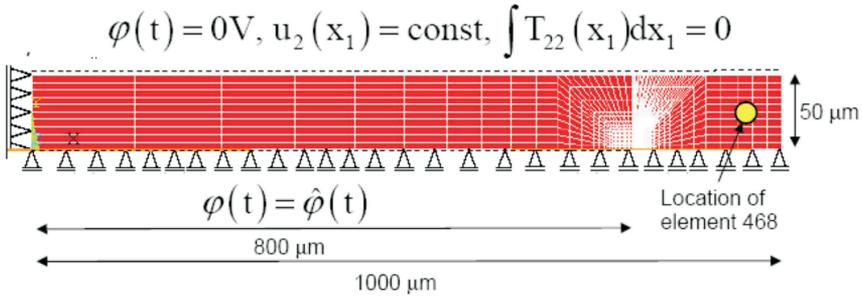
Figure 4. Finite element discretization of a part of the layer of a stack actuator.

of the antisymmetry along this line. This seems to be satisfied as the distance to the field intensification at the electrode tip is much larger than the thickness of the layer. The electrode at the bottom ends at a distance of $200\,\mu$m from the right border. To simulate the poling process of such devices, an electric potential is applied to the top line of the model to reach a maximum voltage of $150\,$V (an average electric field of $3\,$kV/mm). Afterwards the actuator is electrically unloaded.

Figure 5 shows the simulation results of the electric potential at maximum load and after unloading.

For linear simulations with commercial finite element codes, usually a homogeneous polarization state in the vertical direction is assumed. In contrast to this, the poling state in the nonlinear ferroelectric simulations is computed here and not assumed. There is no evolution of irreversible polarization in the region to the right of the tip of the lower electrode, because there is a nearly homogeneous electric potential (see Figure 5a) and, consequently, the tensor of piezoelectricity is still zero (see Equation (4)). After unloading (see Figure 5b) there remains a significant electric potential around the electrode tip which can be explained by the divergence of the irreversible polarization vector in the neighborhood of the tip. Figure 6 shows the irreversible polarization at maximum load around the electrode tip.

Figure 7 shows the distribution of the normal stress in the vertical direction plotted along the bottom line of the model at maximum load and after unloading. At the electrode tip, there is a stress intensification. More importantly, the level of tensile stress in the unpoled area even after unloading remains at $40\,$MPa. This tensile stress is caused by the vertical extension of the active region to the left of the
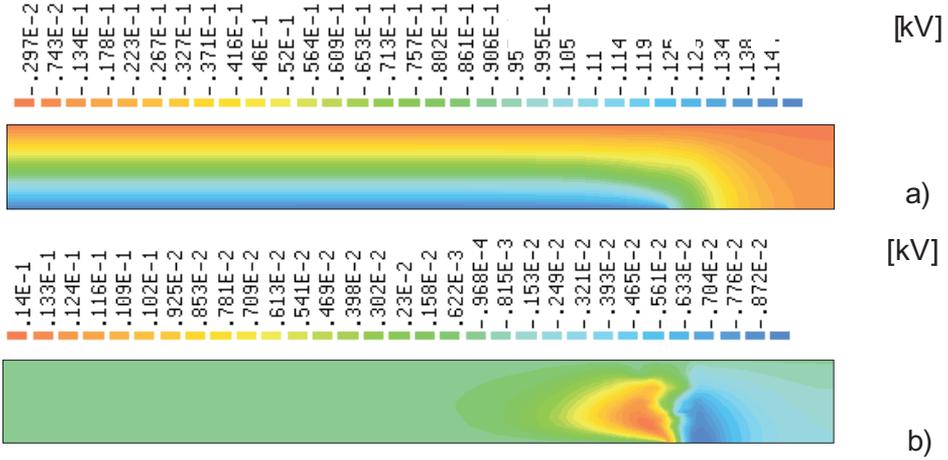
Figure 5. Distribution of the electric potential of a part of a layer of a stack actuator: (a) ferroelectric simulation at maximum voltage and (b) ferroelectric simulation after un-loading.
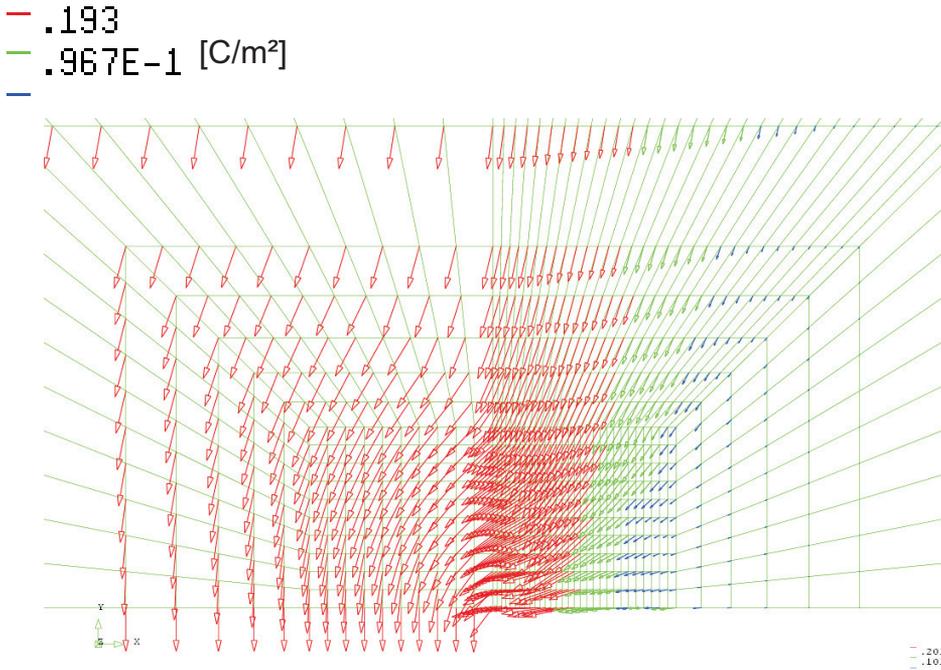
Figure 6. Vector plot of the irreversible polarization around the electrode tip.

electrode tip during poling. By equilibrium, these tensile stresses give rise to compressive stresses along the lower electrode to the left of its tip. For wider actuators with a larger active region of the layer between the electrodes this compressive stress would be smaller. The tensile stresses are in the range of the tensile strength of the material and can lead to cracks while poling the device. Moreover, after poling there is cyclic loading which increases the danger of fatigue because of the residual tensile stress in the
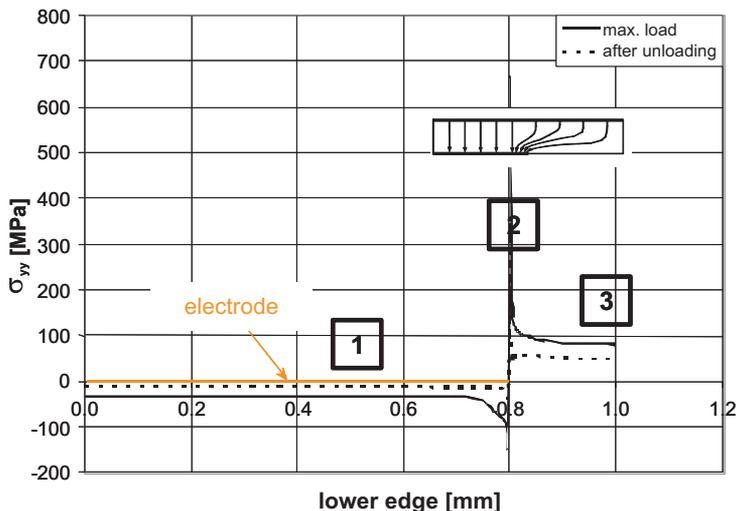
Figure 7. Stress distribution in the vertical direction at the bottom line of the finite element model at maximum load and after unloading.

passive region to the right to the electrode tip. In practice the actuators are prestressed in applications to avoid cracking. By using our finite element tool the magnitude of the prestress and the geometries of the devices may be optimized. On the one hand, the tensile stresses have to be minimized by means of the prestress. On the other hand, too large a prestress has to be avoided, so no mechanical depolarization can occur, which would reduce the performance of the actuator. An optimum between minimal depolarization and minimal tensile stress has to be found.

Further simulation examples from experimental practice can be found in [Laskewitz et al. 2006] (piezo-ceramic thin walled tubes) and [Westram et al. 2007] (electrically driven crack growth).

4. Microscopically motivated material model and its finite element implementation

4.1. *Formulation of the microscopically motivated material model.* In this section, we present a micro-scopically motivated constitutive model for ferroelectrics, the development of which started with [Kamlah and Jiang 1999; Kamlah and Wang 2003]. Just as with the model introduced in the previous section, this model is applied at macroscopic length scales, that is, at the level of engineering components. In contrast to the previous model which is formulated by methods of classical phenomenological modeling, the model in this section relies on quantities of clear micromechanical meaning. For a tetragonal structure of the unit cells, the microscopically motivated model is based on the orientation distribution of lattice axes and spontaneous polarization. A tetragonal unit cell possesses two distinct lattice constants, the c-axis which is up to 1% larger than the other axis, called the a-axis. For each orientation of the c-axis, there are still two possible orientations of the spontaneous polarization, and regions in a grain which have the same orientation of c-axes and spontaneous polarizations are called domains.

As with the phenomenological model, the current model relies on an additive decomposition. However, for the microscopically motivated constitutive model, irreversible strain and polarization themselves are not taken as internal or state variables. Rather, they are assumed to be functions of some microstructural

parameters $q^1, \ldots, q^n$, which represent the microscopic domain state at the macroscopic level, and in this way act as the state variables:

$$S_{ij}^i = S_{ij}^i(q^1, \ldots, q^n), \qquad P_i^i = P_i^i(q^1, \ldots, q^n). \tag{24}$$

The model is based on the Gibbs free energy

$$g = \tfrac{1}{2} T_{ij} C_{ijkl}^{-1} T_{kl} + E_i d_{ijk} T_{jk} + \tfrac{1}{2} E_i \kappa_{ij} E_j + \mathrm{gi}(q^1, \ldots, q^n). \tag{25}$$

By exploiting the Clausius–Duhem inequality, this leads to relations (2) with the definition of the material tensors as before, in particular (3). Furthermore, we obtain the driving forces

$$\phi^\alpha = E_i \frac{\partial P_i^i}{\partial q^\alpha} + T_{ij} \frac{\partial S_{ij}^i}{\partial q^\alpha} + \rho \frac{\partial g}{\partial q^\alpha}, \quad \alpha = 1, \ldots, n, \tag{26}$$

being thermodynamically conjugate to the corresponding state variable q^α. Further details on the thermodynamical framework can be found in [Kamlah and Wang 2003].

By means of a convex switching function $f = f(\phi^1, \ldots, \phi^n)$, which includes the origin, the normality rule

$$\dot{q}^\alpha = \lambda \frac{\partial f}{\partial \phi^\alpha} \tag{27}$$

leads to evolution equations for the state variables which satisfy the dissipation inequality in a sufficient manner. Here, for a rate independent theory, the irreversible multiplier λ can be determined by means of the consistency condition:

$$\lambda \begin{cases} \text{solves } \dot{f} = \sum_{\alpha=1}^n \dfrac{\partial f}{\partial \phi^\alpha} \dfrac{\partial \phi^\alpha}{\partial q^\beta} \dot{q}^\beta = 0 & \text{for } f(\phi^1, \ldots, \phi^n) = 0 \text{ and } \dot{f}\big|_{\dot{q}^1, \ldots, \dot{q}^n = 0} > 0, \\ = 0 & \text{else.} \end{cases} \tag{28}$$

4.1.1. *1D approach.* For a better understanding, the choice of internal state variables of the model is motivated by means of a 1D approach. Figure 8 shows a projection of a unit sphere with two inner cones, where the cones axes are parallel to the loading direction (x_3) and the cones have an opening angle θ^e. The continuous straight lines represent the orientation of selected c-axes and the direction of the spontaneous polarization is indicated by the arrow tips. The sphere represents the distribution of the orientation of c-axes and spontaneous polarization in some representative volume element in the neighborhood of a point in a macrocontinuum. Figure 8b symbolizes the thermally depolarized initial state where the distribution c-axes and spontaneous polarization is uniform over the sphere. For this initial state, the average macroscopic irreversible polarization and strain are zero.

The first state variable to be identified is $q^1 = \beta$, which is the fraction of c-axes within the cones. The range of β is $\beta \in [0; 1]$, in which zero is the case where no c-axes are inside the cones. For $\beta = 1$, all c-axes are within the cones in which case the irreversible strain reaches its saturation value $S_{33}^i = S^{\mathrm{sat}}$. For the initial state of random distribution of the c-axes β assumes its reference value β^{ref}. The opening angle θ^e of the cones and the state variable β can also be interpreted as parameters of a step function approximation of the orientation distribution function (ODF) of the c-axes. This distribution would be transversely isotropic meaning that it is invariant for arbitrary rotations about the axis of loading. The

poloidal variation of this approximate ODF can be written as

$$
p(\theta) = \begin{cases} \dfrac{\beta}{4\pi\,(1-\cos\theta^{\mathrm{e}})} & \text{for } 0 \le \theta \le \theta^{\mathrm{e}} \text{ and } \pi - \theta^{\mathrm{e}} \le \theta \le \pi, \\[2ex] \dfrac{1-\beta}{4\pi\,\cos\theta^{\mathrm{e}}} & \text{for } \theta^{\mathrm{e}} < \theta < \pi - \theta^{\mathrm{e}}, \end{cases} \qquad 0 \le \beta \le 1. \tag{29}
$$

For the initial random state, that is, a uniform distribution of the c-axes, β assumes its reference value $\beta^{\mathrm{ref}} = 1 - \cos\theta^{\mathrm{e}}$. A graphical representation of the ODF is shown in Figure 9 for the range $0 \le \theta \le \frac{\pi}{2}$.

By integration over the approximate ODF [Kamlah and Wang 2003], we obtain immediately

$$
S^{\mathrm{i}}_{33}(\beta) = S^{\mathrm{sat}} \frac{\beta - \beta^{\mathrm{ref}}}{1 - \beta^{\mathrm{ref}}} \tag{30}
$$

for the dependence of irreversible strain on the microstructural parameter β.

For each fixed orientation of the c-axes of a domain, there are still two possible directions for the corresponding spontaneous polarization. From this it is quite obvious, that variable β is not sufficient to describe the macroscopic state within the unit sphere, see Figure 8. Rather, a second state variable
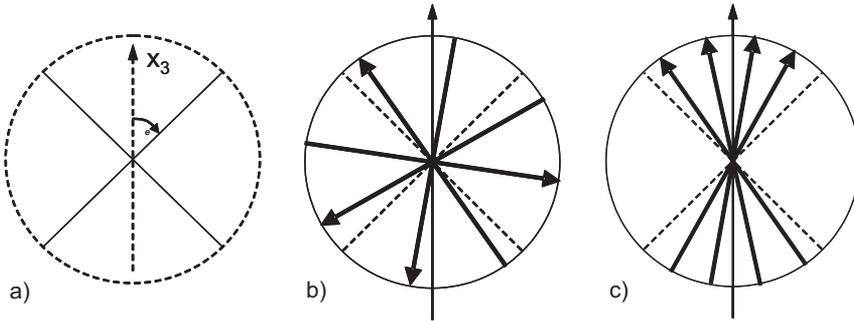
Figure 8. Projection of a sphere with two inner cones around the loading axis x_3.
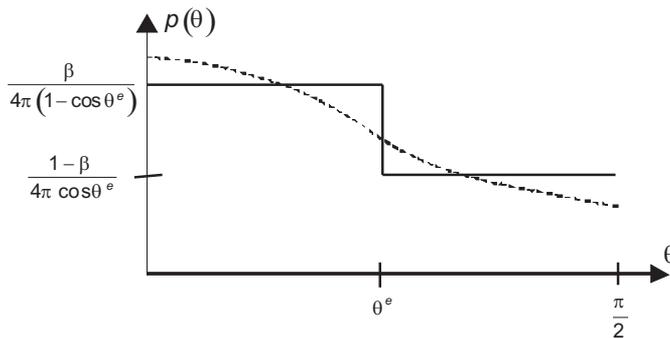
Figure 9. Transversally isotropic ODF $p(\theta)$ for the domain density. The dashed line represents the real function, while the solid line is the simplification used in the material model.

$q^2 = \gamma$ needs to be introduced, describing the relative macroscopic polarization:

$$\gamma = \frac{\| P_i^{\mathrm{i}} \|}{P^{\mathrm{sat}}}. \tag{31}$$

Of course, $\gamma = 0$ holds for the thermally depolarized initial state, as there is no polarization at the macroscopic level. It has to be noted that state variable γ is not completely independent of β. Integration over the approximate ODF [Kamlah and Wang 2003] yields the maximum irreversible polarization belonging to a given orientation state of the c-axes. One obtains

$$\gamma^{\mathrm{max}, \|}(\beta) = \frac{\beta + \cos \theta^{\mathrm{e}}}{1 + \cos \theta^{\mathrm{e}}} = \frac{\beta - \beta^{\mathrm{ref}} + 1}{2 - \beta^{\mathrm{ref}}} \tag{32}$$

for the maximum relative irreversible polarization in the loading direction that can be attained for a given orientation state of the c-axes characterized by β. The maximum or minimum ($\gamma = \pm 1$) can only be reached if all c-axes are within the cones, that is, $\beta = 1$. If all c-axes are outside of the cones, a maximum polarization magnitude of $\gamma^{\mathrm{max}, \|}(0)$ is still possible. For $0 \leq \beta \leq 1$ the maximum irreversible polarization is a function of β:

$$|\gamma| \leq \gamma^{\mathrm{max}, \|}(\beta). \tag{33}$$

Thus, β and γ may assume values only from a range of admissible values defined by

$$G = \left\{ (\beta, \gamma) \,\middle|\, |\gamma| \leq \gamma^{\mathrm{max}, \|}(\beta), 0 \leq \beta \leq 1 \right\}. \tag{34}$$

Figure 10 shows region G with border ∂G which β and γ are not allowed to leave. To compare both, the phenomenological and the microscopically motivated constitutive models, we consider the simple simulation in Figure 11, showing dielectric and butterfly hysteresis, respectively. It clearly can be seen that the evolution of the state variables initiates at reaching the coercive field. After this, the plots of the curves differ significantly. In the microscopically motivated material model, 90 and 180 switching processes and saturation are taken into account more realistically. After reaching the saturation both models follow the linear piezoelectric behavior.

4.1.2. *3D generalization of the material model.* In the following, the material model will be generalized for 3D loadings. Therefore, two additional state variables are introduced. The first one $q^3 = e_i^{\beta}$ is a unit
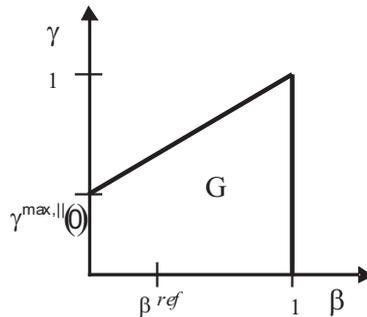
Figure 10. Range G of admissible values for the state variables β and γ.
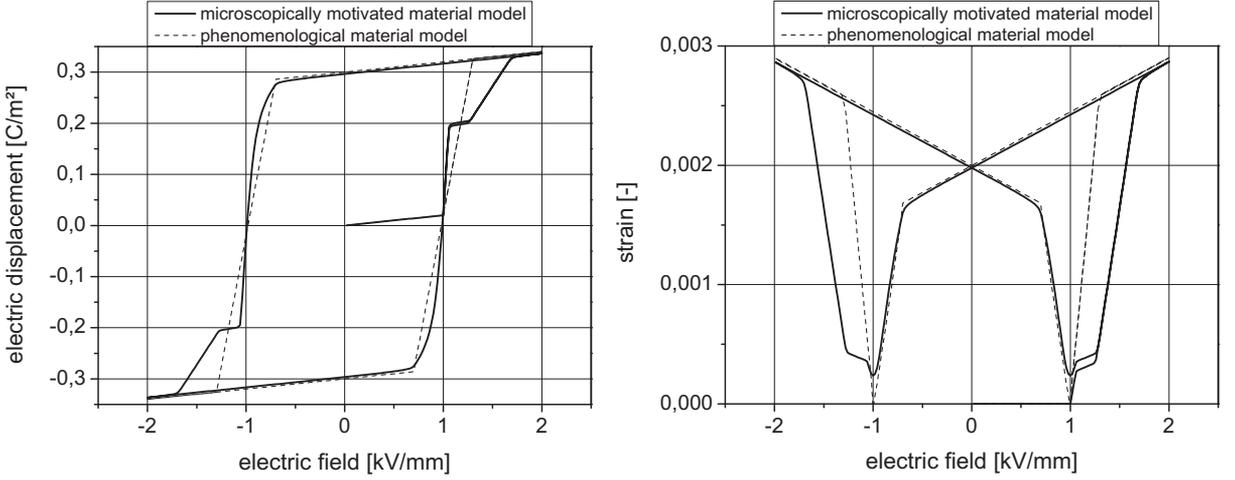
Figure 11. Dielectric and butterfly hysteresis for both material models.

vector representing the direction of the axis of the transversely isotropic ODF in 3D space. This direction depends on the loading history. Then, the irreversible strain is written as

$$S_{ij}^{i} = \frac{3}{2} S^{sat} \frac{\beta - \beta^{ref}}{1 - \beta^{ref}} \left(e_i^{\beta} e_j^{\beta} - \frac{1}{3} \delta_{ij} \right), \tag{35}$$

where δ_{ij} is the Kronecker symbol. This tensor represents an irreversible strain state with a normal strain according to Equation (30) in the direction of unit vector e_i^{β}. The normal strains perpendicular to e_i^{β} then follow from the requirement that the total irreversible strain tensor must be isochoric. This requirement is motivated by switching processes being the underlying mechanism.

Depending on the loading history, the direction of the ODF and the direction of the irreversible polarization need not be the same. Therefore, another unit vectorial state variable $q^4 = e_i^{\gamma}$ is introduced by which the irreversible polarization vector is expressed as $P_i^{i} = \gamma P^{sat} e_i^{\gamma}$.

Since in general e_i^{β} and e_i^{γ} include an angle resulting in $|e_i^{\beta} e_i^{\gamma}| < 1$, the region G of admissible values for our internal variables has to be reformulated. If $e_i^{\beta} = e_i^{\gamma}$, we have $|\gamma| \leq \gamma^{max, \parallel}(\beta)$. If e_i^{β} and e_i^{γ} are perpendicular to each other, one finds $|\gamma| \leq \gamma^{max, \perp}(\beta)$, where $\gamma^{max, \perp}$ is obtained from integration over the ODF [Kamlah and Wang 2003] yielding

$$\gamma^{max, \perp}(\beta) = \frac{\pi - 2\theta^e + \sin 2\theta^e}{\pi \cos \theta^e (1 + \cos \theta^e)} + \left(\frac{2\theta^e - \sin 2\theta^e}{\pi (1 - \cos^2 \theta^e)} - \frac{\pi - 2\theta^e + \sin 2\theta^e}{\pi \cos \theta^e (1 + \cos \theta^e)} \right) \beta. \tag{36}$$

For an arbitrary angle with $0 \leq \cos |e_i^{\beta} e_i^{\gamma}| \leq 1$, the linear interpolation,

$$\gamma^{max}(\beta, e_i^{\beta}, e_i^{\gamma}) = \gamma^{max, \perp}(\beta) + \left(\gamma^{max, \parallel}(\beta) - \gamma^{max, \perp}(\beta) \right) |e_i^{\beta} e_i^{\gamma}|, \tag{37}$$

is used for the maximum magnitude of relative irreversible polarization. In summary, the region of admissible values for the set $\{\beta, \gamma, e_i^{\beta}, e_i^{\gamma}\}$ of internal state variables in 3D reads as

$$G = \left\{ (\beta, \gamma, e_i^{\beta}, e_i^{\gamma}) \mid |\gamma| \leq \gamma^{max}(\beta, e_i^{\beta}, e_i^{\gamma}), 0 \leq \beta \leq 1 \right\}. \tag{38}$$

4.1.3. *3D formulation of the evolution equations.* As a hardening parameter, an energy barrier function is introduced which satisfies the conditions

$$
\begin{aligned}
F^G &\to \infty && \text{for } (\beta, \gamma, e_i^\beta, e_i^\gamma) \to \partial G, \\
F^G &= 0, \quad \frac{\partial F^G}{\partial \beta} = 0, \text{ and } \frac{\partial F^G}{\partial \gamma} = 0 && \text{for } (\beta, \gamma) = (\beta^{\text{ref}}, 0) \text{ and all } (e_i^\beta, e_i^\gamma).
\end{aligned}
\tag{39}
$$

While the first condition implies that the region of admissible values is surrounded by an energy wall of infinite height, the second condition ensures that there is no effect from the energy barrier function F^G in the unpoled initial state. The energy barrier function was chosen as

$$
F^G = A\Big(b(\beta)\big(\beta^{-N} + (1 - \beta)^{-N}\big) + g(\gamma)\big(\gamma^{\max} - |\gamma|\big)^{-N}\Big),
\tag{40}
$$

in which A und N are positive constants and, for example, $b(\beta) = (\beta - \beta^{\text{ref}})^4$ and $g(\gamma) = \gamma^4$ to enforce the second set of conditions (39).

By means of the Gibbs free energy, the driving forces for the internal variables can be obtained from expression (26) as

$$
\begin{aligned}
\phi^\beta &= \frac{3}{2}\frac{S^{\text{sat}}}{1 - \beta^{\text{ref}}}\Big(e_i^\beta e_j^\beta - \frac{1}{3}\delta_{ij}\Big)T_{ij} + \frac{1}{2}\frac{\partial C_{jklm}^{-1}}{\partial \beta}T_{jk}T_{lm} + \frac{1}{2}\frac{\partial \kappa_{jk}}{\partial \beta}E_j E_k - c^\beta(\beta - \beta^{\text{ref}}) - \frac{\partial F^G}{\partial \beta}, \\
\phi^\gamma &= P^{\text{sat}}E_i e_i^\gamma + \frac{\partial d_{kij}}{\partial \gamma}E_k T_{ij} - c^\gamma \gamma - \frac{\partial F^G}{\partial \gamma}, \\
\phi_i^{\vec{e}^\beta} &= 3S^{\text{sat}}\frac{\beta - \beta^{\text{ref}}}{1 - \beta^{\text{ref}}}T_{ij}e_j^\beta + \frac{1}{2}\frac{\partial C_{jklm}^{-1}}{\partial e_i^\beta}T_{jk}T_{lm} + \frac{1}{2}\frac{\partial \kappa_{jk}}{\partial e_i^\beta}E_j E_k - \frac{\partial F^G}{\partial e_i^\beta}, \\
\phi_i^{\vec{e}^\gamma} &= P^{\text{sat}}\gamma E_i + \gamma \frac{\partial d_{krs}^{\text{sat}}}{\partial e_i^\gamma}E_k T_{rs} - \frac{\partial F^G}{\partial e_i^\gamma}.
\end{aligned}
\tag{41}
$$

Since e_i^β and e_i^γ have to remain unit vectors, only the component of the driving force perpendicular to the corresponding unit vector must be taken into account for the respective evolution equation:

$$
\phi_i^{\vec{e}^\beta, \perp} = (\delta_{ij} - e_i^\beta e_j^\beta)\phi_j^{\vec{e}^\beta}, \qquad \phi_i^{\vec{e}^\gamma, \perp} = (\delta_{ij} - e_i^\gamma e_j^\gamma)\phi_j^{\vec{e}^\gamma}.
\tag{42}
$$

This is by analogy to incremental plasticity, where only the stress deviator contributes to the evolution of volume preserving plastic strain.

As a simple choice, the convex switching function is then given by

$$
f = \sqrt{\Big(\frac{\phi^\beta}{\phi^{\beta,0}}\Big)^2 + \Big(\frac{\phi^\gamma}{\phi^{\gamma,0}}\Big)^2 + \Big(\frac{|\vec{\phi}^{\vec{e}^\beta, \perp}|}{\phi^{\vec{e}^\beta,0}}\Big)^2 + \Big(\frac{|\vec{\phi}^{\vec{e}^\gamma, \perp}|}{\phi^{\vec{e}^\gamma,0}}\Big)^2} - 1,
\tag{43}
$$

in which

$$
\phi^{\beta,0} = \frac{S^{\text{sat}}\sigma^{\text{c}}}{1 - \beta^{\text{ref}}}, \qquad \phi^{\gamma,0} = P^{\text{sat}}E^{\text{c}}, \qquad \phi^{\vec{e}^\beta,0} = \sqrt{3}\sigma^{\text{c}}S^{\text{sat}}\frac{\beta - \beta^{\text{ref}}}{1 - \beta^{\text{ref}}}, \qquad \phi^{\vec{e}^\gamma,0} = \gamma P^{\text{sat}}E^{\text{c}}.
\tag{44}
$$

For pure electric loadings, this criterion is satisfied (that is, $f = 0$) if the magnitude of the electric field vector E_i is equal to the coercive field strength E^{c}. For pure mechanical loadings, this switching function is equivalent to a *von Mises* type criterion.

By the normality rule (27), the evolution equations for the internal variables are obtained as

$$
\dot{\beta} = \lambda \frac{\partial f}{\partial \phi^\beta} = \frac{\lambda}{1+f} \left(\frac{1}{\phi^{\beta,0}}\right)^2 \phi^\beta, \qquad\qquad \dot{\gamma} = \lambda \frac{\partial f}{\partial \phi^\gamma} = \frac{\lambda}{1+f} \left(\frac{1}{\phi^{\gamma,0}}\right)^2 \phi^\gamma,
$$
$$
\dot{\vec{\mathrm{e}}}^\beta = \lambda \frac{\partial f}{\partial \phi^{\vec{\mathrm{e}}^\beta}} = \frac{\lambda}{1+f} \left(\frac{1}{\phi^{\vec{\mathrm{e}}^\beta,0}}\right)^2 \vec{\phi}^{\vec{\mathrm{e}}^\beta,\perp}, \qquad \dot{\vec{\mathrm{e}}}^\gamma = \lambda \frac{\partial f}{\partial \phi^{\vec{\mathrm{e}}^\gamma}} = \frac{\lambda}{1+f} \left(\frac{1}{\phi^{\vec{\mathrm{e}}^\gamma,0}}\right)^2 \vec{\phi}^{\vec{\mathrm{e}}^\gamma,\perp}.
$$

$$(45)$$

This system of eight ordinary differential equations has to be solved in the finite element implementation. To remove redundant equations, the formulation of the material law was rewritten in generalized variables, where the unit vectors are represented by two polar variables instead of three cartesian components [Laskewitz 2007].

4.2. *Finite element implementation.*

First of all, coming from the elastic region, initial values for the state variables e_i^β and e_i^γ have to be found before switching starts for the first time. Several cases have to be taken into consideration, which are presented in Table 3.

Due to the nonlinearity of the problem, the loading history is subdivided into increments. In the following, we consider the general case of a computation for some time instant $^{n+1}t = t + \Delta t$. We depart from some known state at time $^{n}t = t$ (the last increment), meaning the state variables $^{n}q^\alpha$ are known (besides strain $^{n}S_{ij}$ and electric field $^{n}E_i$, of course). Furthermore, trial values $^{n+1}S_{ij}$ and $^{n+1}E_i$ for strain and electric field, respectively, are given from the global Newton iteration. The task is to find the state variables $^{n+1}q^\alpha$ from which the stress $^{n+1}T_{ij}$ and the electric displacement $^{n+1}D_i$ can be computed. Furthermore, the algorithmic consistent tangents

$$
{}^{n+1}\left(\frac{\partial D_i}{\partial E_j}\right), \quad {}^{n+1}\left(\frac{\partial T_{ij}}{\partial E_k}\right), \quad {}^{n+1}\left(\frac{\partial D_i}{\partial S_{jk}}\right), \quad {}^{n+1}\left(\frac{\partial T_{ij}}{\partial S_{kl}}\right),
$$

have to be provided to guarantee quadratic convergence of the global Newton iteration.

Case	Initial value
$\|^{n+1}T_{ij}^{\mathrm{rev}}\| = 0$ and $\|^{n+1}E_i\| = 0$	Undefined
$\|^{n+1}T_{ij}^{\mathrm{rev}}\| = 0$ and $\|^{n+1}E_i\| > 0$	$e_i^\beta = \dfrac{^{n+1}E_i}{\|^{n+1}E_i\|} \; e_i^\gamma = \dfrac{^{n+1}E_i}{\|^{n+1}E_i\|}$
$\|^{n+1}T_{ij}^{\mathrm{rev}}\| > 0$ and $\|^{n+1}E_i\| = 0$	e_i^β, e_i^γ : eigenvector of $^{n+1}T_{ij}^{\mathrm{rev}}$ belonging to largest eigenvalue
$\|^{n+1}T_{ij}^{\mathrm{rev}}\| > 0$ and $\|^{n+1}E_i\| > 0$	e_i^β : eigenvector of $^{n+1}T_{ij}^{\mathrm{rev}} \; e_i^\gamma = \dfrac{^{n+1}E_i}{\|^{n+1}E_i\|}$

Table 3. Initial values for e_i^β and e_i^γ ($^{n+1}T_{ij}^{\mathrm{rev}}$ is the elastic stress tensor (trial stress) at the end of the increment).

The bases for this computation are the evolution equations (27) which are solved by a backward Euler scheme yielding

$$^{n+1}q^\alpha(t+\Delta t) = {}^nq^\alpha(t) + \Delta t \cdot {}^{n+1}\lambda(t+\Delta t)\,{}^{n+1}\!\left(\frac{\partial f}{\partial\phi^\alpha}\big(q^\beta(t+\Delta t), t+\Delta t\big)\right). \tag{46}$$

By means of the notation $^{n+1}q^\alpha = q^\alpha(t+\Delta t)$ and $^{n+1}\lambda = \lambda(t+\Delta t)$ for the state variables and the so-called irreversible multiplier, (46) can be rewritten as

$$F^\alpha = q^\alpha(t+\Delta t) - q^\alpha(t) - \Delta t\,\lambda(t+\Delta t)\frac{\partial f}{\partial\phi^\alpha}\big(q^\beta(t+\Delta t), t+\Delta t\big) = 0. \tag{47}$$

The switching condition

$$f\big(q^\alpha(t+\Delta t), t+\Delta t\big) = 0. \tag{48}$$

completes the system of equations.

From Taylor series expansion and linearization of functions F^α and f, the iteration scheme

$$
\begin{aligned}
{}^{j+1}F^\alpha &= {}^jF^\alpha + {}^j\!\left(\frac{\partial F^\alpha}{\partial q^\beta}\right)\cdot{}^{j+1}\delta q^\beta + {}^j\!\left(\frac{\partial F^\alpha}{\partial\lambda}\right)\cdot{}^{j+1}\delta\lambda = 0, \\
{}^{j+1}f &= {}^jf + {}^j\!\left(\frac{\partial f}{\partial q^\alpha}\right)\cdot{}^{j+1}\delta q^\alpha = 0,
\end{aligned}
\tag{49}
$$

can be found in which

$$^jF^\alpha = {}^jq^\alpha - q^\alpha(t) - \Delta t \cdot {}^j\lambda\frac{\partial f}{\partial\phi^\alpha}({}^jq^\beta, t+\Delta t), \qquad {}^jf = f({}^jq^\alpha, t+\Delta t). \tag{50}$$

This procedure is equivalent to the Newton–Kantorovich method. As a consequence, a second local Newton iteration has been established to solve the constitutive law at each integration station in each load step.

To achieve quadratic convergence in the global Newton iteration during nonlinear computation of switching processes, it is necessary to employ the so-called algorithmic consistent tangent moduli. For such a complex constitutive model as the one considered in this paper, it is not possible to derive these moduli in closed form. Approximations may be used, such as the material tensors from the linear constitutive law, yielding a quasi-Newton method with only linear convergence guaranteed. Otherwise, numerical differentiation may be employed:

$$
\begin{aligned}
^{n+1}\!\left(\frac{\partial D_i}{\partial E_j}\right) &= \frac{D_i(E_j+h) - D_i(E_j)}{h}, & ^{n+1}\!\left(\frac{\partial T_{ij}}{\partial E_k}\right) &= \frac{T_{ij}(E_k+h) - T_{ij}(E_k)}{h}, \\
^{n+1}\!\left(\frac{\partial D_i}{\partial S_{jk}}\right) &= \frac{D_i(S_{ik}+h) - D_i(S_{ik})}{h}, & ^{n+1}\!\left(\frac{\partial T_{ij}}{\partial S_{kl}}\right) &= \frac{T_{ij}(S_{kl}+h) - T_{ij}(S_{kl})}{h},
\end{aligned}
\tag{51}
$$

in which $h = \sqrt{eps} \approx 1,5\cdot10^{-8}$ should be chosen, where *eps* is the accuracy of the computer.

4.2.1. *Methods to improve convergence.* In the finite element solution, occasional convergence problems occurred. This section describes some methods to enhance the convergence of the finite element implementation. The convergence problems occur mainly because of the form of the energy barrier function which is a hyperbola. There is a possibility for the state variables to take values outside the region of

admissible values because of inaccuracies during the iteration procedures. In this case, a physically incorrect solution is obtained. Therefore, it should be ensured that the state variables cannot leave the region of admissible values. The Newton method needs a start vector which is sufficiently close to the solution for an accurate convergence to the physically correct roots of the system (47)–(48). To improve convergence, several methods have been studied and tested. An overview of the most important methods is given in Table 4. It has to be mentioned that sometimes convergence still could not be achieved.

4.2.2. *Verification of the implementation of the microscopically motivated material model.* Based on the material parameters in Table 5, the microscopically motivated constitutive model and its finite element implementation are verified in comparison to experimental results.

Figure 12 shows the dielectric and the butterfly hysteresis from experiments and simulations. The microscopically motivated model can represent the material behavior very well.

4.3. *Simulation example: hollow cylinder.* In experiments, hollow cylinders are often used to investigate multiaxial loading states. Figure 13a shows a piezoceramic circular ring which is poled in the radial direction. The axisymmetric finite element model shown in Figure 13b represents a cylinder of infinite axial length, since all vertical displacements at the top of the model are forced to be equal. The maximum electric potential loading is equivalent to an average electric field of $3E^c$. Following poling, the cylinder is unloaded again. The material parameters are adjusted to a soft lead-zirconate-titanate (soft PZT) and are presented in Table 6.

Figure 14 presents the deformed and undeformed finite element mesh. The electrical loading induces a decrease of the inner radius accompanied by a shortening in the vertical direction in comparison to the

Method to improve convergence	Advantages and disadvantages
Consistent tangent moduli	+ Improvement of global convergence + In general local convergence better − Computationally expensive
Enforcing admissible range for β and γ	+ Improvement of convergence − Limitation in finding suitable start vectors
Damped Newton method for local Newton iteration	+ Significant improvement of convergence + Computationally inexpensive − Strong dependence on the maximum number of iterations for the damped local Newton method (different roots can be found for different maximum numbers of iterations)
Systematic search for suitable start vector (Euler forward, linear interpolation)	+ Improvement of convergence − Can be computationally expensive
Subincrementing the time step, solution with backward Euler method or forward Euler method	+ Significant improvement of convergence − Computationally very expensive

Table 4. Methods to improve convergence of the Newton method.

E^c (MV/mm)	1.0×10^3
P^{sat} (kN/(MVmm))	310×10^{-3}
σ^c (kN/mm²)	40.0×10^{-3}
S^{sat}	0.00225
Y (kN/mm²)	60.0
ν	0.37
$d^{\parallel}$ (mm/MV)	6.75×10^{-1}
$d^{\perp}$ (mm/MV)	-3.15×10^{-1}
$d^{=}$ (mm/MV)	4.35×10^{-1}
c^{γ} (kN/mm²)	3.0×10^{-5}
c^{β} (kN/mm²)	1.0×10^{-4}
N	2.0
A (kN/mm²)	5.0×10^{-11}

Table 5. Material parameters for the microscopically motivated material model.
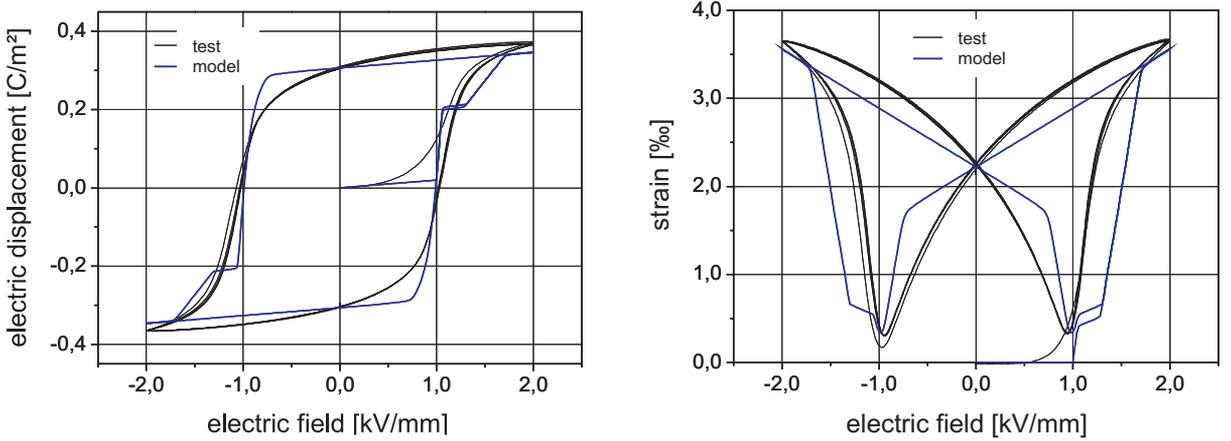
Figure 12. Dielectric (left) and butterfly hysteresis (right) from experiments and simulations.
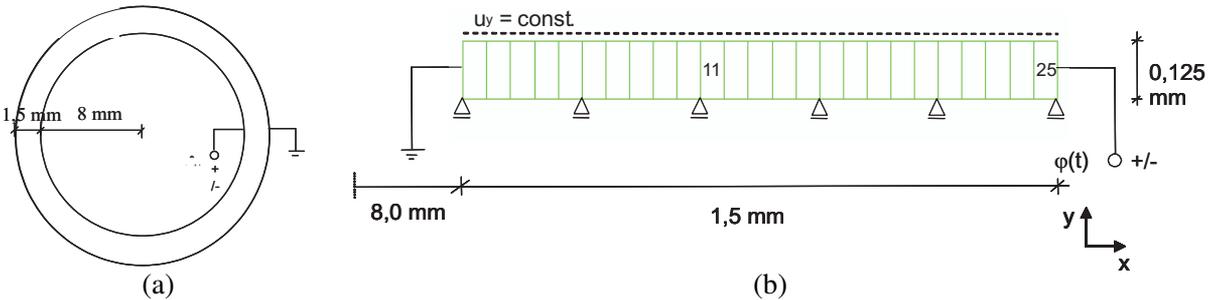
Figure 13. (a) Radial poled circular cylinder, top view, and (b) axisymmetric finite element model.

Y (GPa)	60.0
ν	0.396
σ^{c} (MPa)	40.0
S^{sat}	0.002
E^{c} (kV/mm)	1.0
P^{sat} (C/m^2)	0.29
d_{33} (mm/MV)	4.5×10^{-1}
d_{31} (mm/MV)	-2.1×10^{-1}
d_{15} (mm/MV)	5.8×10^{-1}

Table 6. Material parameters used in the simulations.
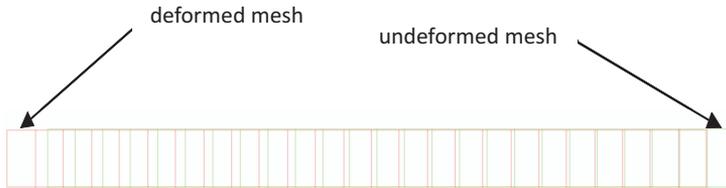
Figure 14. Undeformed and deformed finite element mesh (scale factor 5.27).
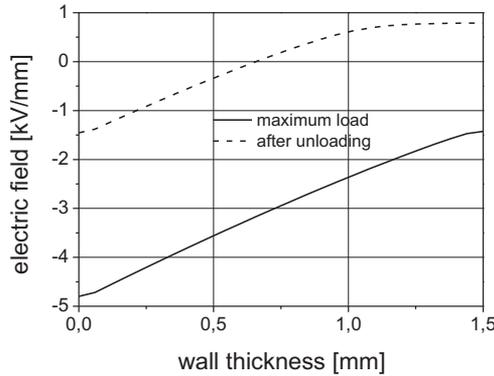
Figure 15. Electric field in the radial direction at maximum load and after unloading over the wall thickness.

initial state. In Figure 15, the electric field versus the wall thickness at the maximum electric potential and after unloading is depicted. At the inner surface of the cylinder the local electric field reaches approximately -5 kV/mm, while at the outer surface, it is just above the coercive field at maximum load. After unloading, there remains a local electric field at the inner surface of approximately -1.5 kV/mm. In contrast to this, the local electric field at the outer surface changes sign and is just below the initial critical field strength for the onset of switching, that is, E^{c}.

In Figure 16 the axial stress over the wall thickness is presented. The distribution of the axial stress is almost linear at maximum voltage. At the inner surface of the cylinder, there are tensile stresses, while at the outer surface there are compressive stresses. The tensile stress is in the range of the tensile strength
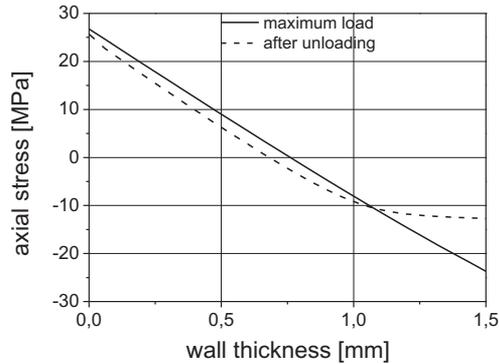
Figure 16. Axial stress over the wall thickness at maximum load and after unloading.
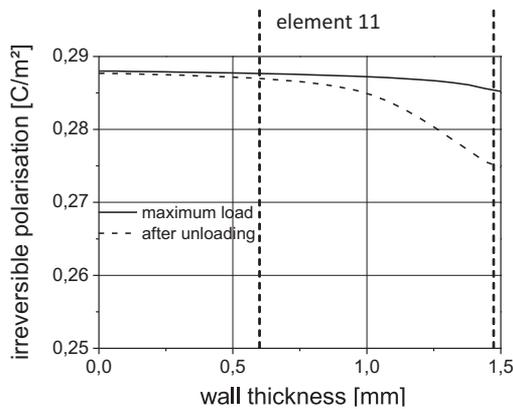
Figure 17. Irreversible polarization over wall thickness at maximum load and after unloading.

of the material and may lead to cracks. After unloading, there remain stresses in the cylinder. At the inner surface there is almost no reduction of the stresses, but at the outer surface, there is a decrease in the axial stresses observed. Because of the inhomogeneous distribution of the electric field, the coercive field is reached earlier in regions near the inner surface initiating domain switching in the radial direction while at the outer surface the coercive field has not yet been reached. This leads to compressive axial stresses close to the outer surface and, as a consequence of equilibrium, to tensile axial stresses near the inner surface. The circumferential stresses (not shown) exhibit a nonlinear distribution as well and do not vanish after unloading. The radial stresses are approximately zero.

Figure 17 shows the irreversible polarization at maximum voltage and after unloading. At maximum load, the saturation polarization is almost reached in all regions of the cylinder. Only at the outer surface, there is a small decrease observed. During unloading the irreversible polarization is decreasing especially at the outer surface. While the stresses in the cylinder wall are significant, they can not explain this effect by means of some mechanical depolarization. As they are compressive, these stresses rather would stabilize the poled state close to the outer surface. To have a closer look at the depolarization effect, the local electric displacement over the local electric field is depicted in Figure 18 for two elements. Element 11 is approximately at the position where the electric field is zero after unloading. Element 25 is at the outer surface of the cylinder (see Figure 17).
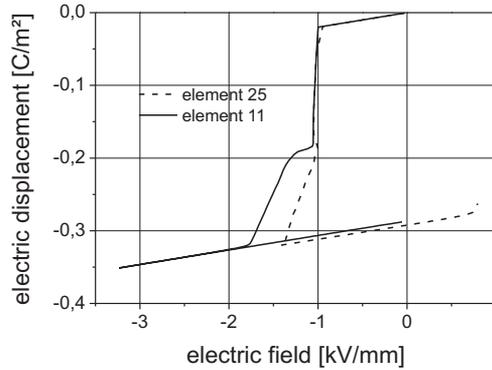
Figure 18. Local electric displacement over local electric field for two positions in the cylinder wall.

In element 11, saturation of the local irreversible polarization is clearly reached, while for element 25 the saturation level is just touched. After unloading, the local electric field in element 11 is reduced to nearly zero, while the local electric displacement approaches P^{sat} as the linear dielectric contribution vanishes. In contrast to this, the local electric field in element 25 changes sign and takes significant values in the opposite direction of the initial poling. As a matter of fact, it reaches the critical electric field for the onset of electrically induced repoling in opposite direction. Around this critical field strength, small changes of the electric field lead to significant changes in the irreversible polarization. Due to the large slope of the polarization changing parts of the hysteresis electrical depolarization takes place. Because of that, after unloading, an obvious reduction of the irreversible polarization is observed near the outer surface of the cylinder, though the electric field is nearly constant with respect to position in this region. The actual critical field strength for the repoling process is dependent on the previous loading history. In particular, it has been reduced close to the outer surface compared to the initial coercive field strength E^{c} due to what we may call a ferroelectric Bauschinger effect. As a consequence, even an arbitrarily high electric voltage during poling is not able to ensure fully saturated polarization over the whole wall thickness after unloading.

By means of this simulation example it could be shown that the implementation of the microscopically motivated material model is very powerful. It can describe the polarization behavior of piezoceramic materials in more detail than the phenomenological model. This statement results from a comparison to simulations in [Laskewitz et al. 2006], where the finite element analysis of piezoceramic hollow cylinders based on the phenomenological model is presented.

5. Conclusion

After motivating this work and giving an overview of the state of the art in the literature, a phenomenological constitutive model for ferroelectrics and its finite element implementation was described. A customized, computationally time efficient integration algorithm (radial return mapping method) was introduced. The model and its finite element implementation was verified by simulation examples and comparison to experiments. As a simulation example, poling of a stack actuator was considered showing the capability of the finite element tool.

Next, a microscopically motivated constitutive model and its finite element implementation by a more complex radial return mapping algorithm was described and verifications by means of experimental data were performed. Lastly, a simulation example using a hollow cylinder showed the applicability of the this finite element tool for practical problems.

In summary, the phenomenological material model is well suited to simulate realistically the overall behavior of large systems. The microscopically motivated material model has its field of application in simulating the detailed electromechanically fields of smaller piezoceramic (sub)systems, because of the higher computation time consumed by the more complex integration algorithm.

References

[Allik and Hughes 1970] H. Allik and T. J. R. Hughes, "Finite element method for piezoelectric vibration", *Int. J. Numer. Meth. Eng.* **2** (1970), 151–157.

[Belov and Kreher 2005] A. Y. Belov and W. Kreher, "Viscoplastic models for ferroelectric ceramics", *J. Eur. Ceramic Soc.* **25**:12 (2005), 2567–2571.

[Boehle 1999] U. Boehle, "Phänomenologische Modellierung und Finite-Elemente-Simulationen von nichtlinearen elektromechanischen Vorgängen in ferroelektrischen Materialien", technical report FZKA 6347, Forschungszentrum Karlsruhe, 1999.

[Chen 1980] P. J. Chen, "Three dimensional dynamic electromechanical constitutive relations for ferroelectric materials", *Int. J. Solids Struct.* **16** (1980), 1059–1067.

[Chen and Lynch 1998] W. Chen and C. S. Lynch, "A micro-electro-mechanical model for polarization switching of ferroelectric materials", *Acta Mater.* **46** (1998), 5303–5311.

[Chen et al. 1997] X. Chen, D. N. Fang, and K. C. Hwang, "Micromechanics simulation of ferroelectric polarization switching", *Acta Mater.* **45** (1997), 3181–3189.

[Delibas et al. 2005] B. Delibas, A. Arockiarajan, and W. Seemann, "A nonlinear model of piezoelectric polycrystalline ceramics under quasi-static electromechanical loading", *J. Materials Science: Materials in Electronics* **16** (2005), 507–515.

[Elhadrouz et al. 2005a] M. Elhadrouz, T. B. Zineb, and E. Patoor, "Constitutive law for ferroelastic and ferroelectric piezoceramics", *J. Intell. Mater. Syst. Struct.* **16** (2005), 221–236.

[Elhadrouz et al. 2005b] M. Elhadrouz, T. B. Zineb, and E. Patoor, "Finite element modeling of piezoelectric actuators and sensors: local analysis of the ferroelectric and ferroelastic effects", in *Proceedings of MRS Spring Meeting* (San Francisco, 2005), vol. CC4.7, edited by R. M. McMeeking et al., 2005.

[Huber and Fleck 2001] J. E. Huber and N. A. Fleck, "Multi-axial electrical switching of a ferroelectric theory vs. experiment", *J. Mech. Phys. Solids* **49** (2001), 785–811.

[Huber and Fleck 2004] J. E. Huber and N. A. Fleck, "Ferroelectric switching: a micromechanics model versus measured behaviour", *Eur. J. Mech. A/Solids* **23** (2004), 203–217.

[Huber et al. 1998] J. E. Huber, N. A. Fleck, C. M. Landis, and R. M. McMeeking, "Constitutive model of ferroelectrics", *J. Mech. Phys. Solids* **47** (1998), 1663–1697.

[Hwang 2000] S. Hwang, "Switching in ferroelectric polycrystals", *J. Appl. Physics* **87** (2000), 869–875.

[Hwang et al. 1995] S. C. Hwang, C. S. Lynch, and R. M. McMeeking, "Ferroelectric/ferroelastic interactions and a polarization switching model", *Acta Metall. Mater.* **43** (1995), 2073–2084.

[Hwang et al. 1998] S. C. Hwang, S. C., and R. M. McMeeking, "A finite element model of ferroelectric polycrystals", *Ferroelectrics* **211** (1998), 177–194.

[Kamlah 2001] M. Kamlah, "Ferroelectric and ferroeleastic piezoceramics: modeling of electromechanical hysteresis phenomena", *Continuum Mech. Thermodyn.* **13** (2001), 219–268.

[Kamlah and Boehle 2001] M. Kamlah and U. Boehle, "Finite element analysis of piezoceramic components taking into account ferroelectric hysteresis behaviour", *Int. J. Solids Struct.* **38** (2001), 605–633.

[Kamlah and Jiang 1999] M. Kamlah and Q. Jiang, "A constitutive model for ferroelectric ceramics under uniaxial loading", *Smart Materials Struct.* **9** (1999), 441–451.

[Kamlah and Tsakmakis 1999] M. Kamlah and C. Tsakmakis, "Phenomenological modeling of the non-linear electro-mechanical coupling in ferroelectrics", *Int. J. Solids Struct.* **36** (1999), 669–695.

[Kamlah and Wang 2003] M. Kamlah and Z. Wang, "A thermodynamically and microscopically motivated constitutive model for piezoceramics", technical report FZKA 6880, Forschungszentrum Karlsruhe, 2003.

[Kamlah et al. 2005] M. Kamlah, A. C. Liskowsky, R. M. McMeeking, and H. Balke, "Finite element simulation of a polycrystalline ferroelectric based on a multidomain single crystal switching model", *Int. J. Solids Struct.* **42** (2005), 2949–2964.

[Kessler and Balke 2001] H. Kessler and H. Balke, "On the local and average energy release in polarization switching phenomena", *J. Mech. Phys. Solids* **49** (2001), 953–978.

[Klinkel 2006] S. Klinkel, "A thermodynamic consistent 1D model for ferroelastic and ferroelectric hysteresis effects in piezoceramics", *Comm. Numer. Meth. Eng.* **22** (2006), 727–739.

[Landis 2002] C. M. Landis, "Fully coupled, multi-axial, symmetric constitutive laws for polycrystalline ferroelectric ceramics", *J. Mech. Phys. Solids* **50** (2002), 127–152.

[Laskewitz 2007] B. Laskewitz, "Finite-Elemente-Implementierung konstitutiver nichtlinearer Stoffgesetze für piezokeramische Werkstoffetitle", technical report FZKA 7359, Forschungszentrum Karlsruhe, 2007.

[Laskewitz and Kamlah 2004] B. Laskewitz and M. Kamlah, "Nonlinear Finite Element Simulations of Poling Processes in Piezoceramic Devices", *Proceedings in Appl. Math. Mech.* **4**:1 (2004), 286–287.

[Laskewitz et al. 2006] B. Laskewitz, M. Kamlah, and C. Chen, "Investigations of the nonlinear behavior of piezoceramic hollow cylinders", *J. Intell. Mater. Syst. Struct.* **17** (2006), 521–532.

[McMeeking and Landis 2002] R. M. McMeeking and C. M. Landis, "A phenomenological multi-axial constitutive law for switching in polycrystalline ferroelectric ceramics", *Int. J. Eng. Sci.* **40** (2002), 1553–1577.

[PSU 2000] PSU, Open-source finite element code, Institut für Statik und Dynamik in der Luft- und Raumfahrttechnik, Universität Stuttgart, 2000.

[Schroeder and Gross 2004] J. Schroeder and D. Gross, "Invariant formulation of the electromechanical enthalpy function of transversely isotropic piezoelectric materials", *Arch. Appl. Mech.* **73** (2004), 533–552.

[Schroeder and Romanowski 2005] J. Schroeder and H. Romanowski, "A thermodynamically consistent mesoscopic model for transversely isotropic ferroelectric ceramics in a coordinate-invariant setting", *Arch. Appl. Mech.* **74** (2005), 863–877.

[Seemann et al. 2004] W. Seemann, A. Arockiarajan, and B. Delibas, "Micromechanical simulation of piezoelectric materials using probability functions", 5387 (2004), 402–410.

[Semenov et al. 2006] A. S. Semenov, H. Kessler, A. Liskowsky, and H. Balke, "On a vector potential formulation for 3D electromechanical finite element analysis", *Comm. Numer. Meth. Eng.* **22** (2006), 357–375.

[Smith et al. 2003] R. C. Smith, S. Seelecke, Z. Ounaies, and J. Smith, "A free energy model for hysteresis in ferroelectric materials", *J. Intell. Mater. Syst. Struct.* **14** (2003), 719–739.

[Westram et al. 2007] I. Westram, B. Laskewitz, D. Lupascu, M. Kamlah, and J. Rödel, "Electric-field-induced crack initiation from a notch in a ferroelectric ceramic", *J. Amer. Ceramic Soc.* **90**:9 (2007), 2849–2854.

[Zhou et al. 2005a] D. Zhou, M. Kamlah, and D. Munz, "Effects of bias electric fields on the non-linear ferroelastic behavior of soft lead zirconate titanate piezoceramics", *J. Amer. Ceramic Soc.* **88** (2005), 867–874.

[Zhou et al. 2005b] D. Zhou, M. Kamlah, and D. Munz, "Effects of uniaxial prestress on the ferroelectric hysteretic response of soft PZT", *J. Eur. Ceramic Soc.* **25** (2005), 425–432.

BERND LASKEWITZ: laskewitz@imf.fzk.de
Karlsruhe Institute of Technology, Institute for Materials Research II, P.O. Box 3640, 76021 Karlsruhe, Germany
http://www.fzk.de/imf2

MARC KAMLAH: marc.kamlah@kit.edu
Karlsruhe Institute of Technology, Institute for Materials Research II, P.O. Box 3640, 76021 Karlsruhe, Germany
http://www.fzk.de/imf2